RSC Advances

ROYAL SOCIETY OF CHEMISTRY

PAPER

View Article Online
View Journal | View Issue

Check for updates

Cite this: *RSC Adv.*, 2024, **14**, 27634

Comparative study of metal–organic frameworks synthesized *via* imide condensation and coordination assembly†

Qiao Liu, ‡ Jordon S. Hilliard, Zhongzheng Cai § and Casey R. Wade *

A series of metal–organic frameworks (**1-XDI**) have been synthesized by imide condensation reactions between an amine-functionalized pentanuclear zinc cluster, $Zn_4Cl_5(bt\text{-}NH_2)_6$, ($bt\text{-}NH_2$ = 5-aminobenzotriazolate), and organic dianhydrides (pyromellitic dianhydride (PMDA), naphthalenetetracarboxylic dianhydride (NDA), 3,3′,4,4′-biphenyltetracarboxylic dianhydride (BPDA) and 4,4′-(hexafluoroisopropylidene)diphthalic anhydride (HFIPA)). The properties of the **1-XDI** MOFs have been compared with analogues (**2-XDI**) prepared using traditional coordination assembly. The resulting materials have been characterized by ATR-IR spectroscopy, acid-digested ^1H NMR spectroscopy, elemental analysis, and gas adsorption measurements. N_2 adsorption isotherm data reveal modest porosities and BET surface areas (30–552 $m^2\ g^{-1}$). All of the new **1-XDI** and **2-XDI** MOFs show selective adsorption of C_2H_2 over CO_2 while **2-PMDI** and **2-BPDI** exhibit high selectivity toward C_3H_6/C_3H_8 separation. This study establishes imide condensation of preformed metal–organic clusters with organic linkers as a viable route for MOF design.

Received 31st July 2024
Accepted 23rd August 2024

DOI: 10.1039/d4ra05563b

rsc.li/rsc-advances

Introduction

The advent of metal–organic frameworks (MOFs) and covalent organic frameworks (COFs) has stimulated intense interest in the design and study of new porous materials for applications in gas separation,[1–3] heterogeneous catalysis,[4,5] and energy storage.[6,7] Porous materials are typically classified based on their structure, composition, and method of self-assembly. For example, MOFs are a subset of coordination polymers (CPs) characterized by 2D or 3D extended structures containing coordination compounds (*i.e.* metal–ligand bonds) and the potential for guest-accessible porosity. Reversible coordinative bond formation during MOF self-assembly often results in highly crystalline products, but crystallinity is not requisite based on the IUPAC definition.[8] The intrinsic disorder in amorphous MOFs limits precise structural characterization, making them less appealing for fundamental studies. Nevertheless, amorphous MOFs often exhibit gas accessible porosity and relatively high surface areas and have gained increasing attention for a range of applications.[9–12] COFs rely on condensation reactions between organic building units to form covalent linkages such as boroxines, imines, triazines, or a variety of other functional groups[13,14] Crystallinity is considered to be a distinguishing feature of COFs among other types of porous organic materials.[15,16] Recently, hybrid materials such as metal-covalent organic frameworks (MCOFs) have emerged.[17] MCOFs begin to blur the lines between the MOF and COF distinctions by utilizing covalent bond formation between organic linker groups and preformed metal coordination compounds for self-assembly (Table S1†).[18–27] MOFs assembled from pentanuclear Zn benzotriazolate clusters, also known as Kuratowski-type clusters, have garnered significant attention for applications in CO_2 capture,[28–32] gas separation,[33–35] catalysis,[36–41] and small-molecule binding and activation.[42–47] Although Kuratowski-type clusters are readily synthesized as discrete molecular species, they have not proven to be broadly accessible in MOF self-assembly reactions. As a result, only a relatively small number of MOFs containing Kuratowski-type clusters have been reported.[48–55] This synthetic difficulty has motivated us to explore alternative synthetic routes for the assembly of porous materials containing Kuratowski-type clusters.

Herein, we describe the synthesis and gas adsorption properties of a series of Zn benzotriazolate MOFs assembled using either imide condensation (**1-XDI**) or traditional coordination assembly (**2-XDI**, Scheme 1). The imide route relies on condensation of commercially available organic dianhydrides with an amine-functionalized Kuratowski-type cluster (**1-NH₂**, Scheme 1). Although this method of self-assembly resembles

---

Department of Chemistry and Biochemistry, The Ohio State University, 100 West 18th Ave, Columbus, OH 43210, USA. E-mail: wade.521@osu.edu

† Electronic supplementary information (ESI) available: Spectroscopic (NMR, ATR-IR, ESI-MS), crystallographic (PXRD), thermogravimetric (TGA), gas adsorption, and elemental analyses. See DOI: https://doi.org/10.1039/d4ra05563b

‡ Present address: Materials Physics and Applications Division, Los Alamos National Laboratory, Los Alamos, NM 87545, USA.

§ Present address: National Engineering Laboratory of Eco-Friendly Polymeric Materials (Sichuan), College of Chemistry, Sichuan University, Chengdu 610064, China.

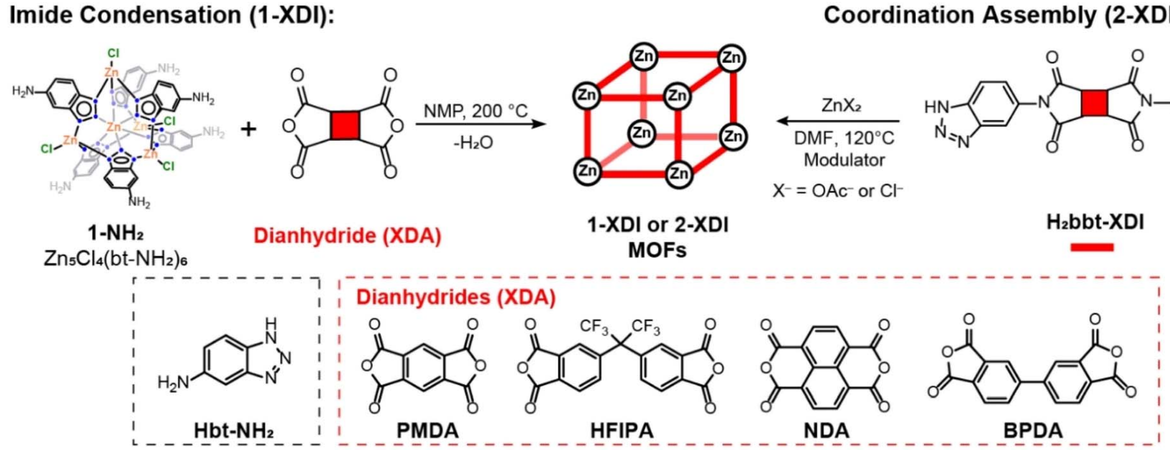

Scheme 1 Synthetic routes to **1-XDI** and **2-XDI** MOFs.

MCOFs, the resulting materials are aptly categorized as MOFs given their composition and guest-accessible porosity. Moreover, three of the four new **1-XDI** MOFs are found to be amorphous, but exhibit modest Brunauer–Emmett–Teller (BET) surface areas and adsorb CO_2 and light hydrocarbon gases at room temperature. A traditional MOF solvothermal synthesis, or coordination assembly route, employing *bis*-benzotriazolate linkers (**H_2bbt-XDI**) and Zn salts has been used to screen the synthesis of an analogous series of MOFs (**2-XDI**). This route also affords amorphous or poorly crystalline products that exhibit gas accessible porosity. Comparison of the **1-XDI** and **2-XDI** MOFs provides insight into the influence of the different synthetic methods on the composition and gas adsorption properties of the resulting porous materials.

Results and discussion

Synthesis and characterization of 1-XDI MOFs

The amine-functionalized Kuratowski cluster **$1\text{-}NH_2$** [$Zn_5Cl_4(bt\text{-}NH_2)_6$] was prepared from reaction of 5-aminobenzotriazole (Hbt-NH_2) with $ZnCl_2$ according to a modified literature procedure (Scheme 1).[56] **$1\text{-}NH_2$** was obtained as an amorphous, pale yellow solid and characterized by electrospray ionization mass spectrometry (ESI-MS, positive ion mode) and ^1H NMR spectroscopy. The former shows a series of ion signals in the m/z = 1230–1480 range that correspond to acetone and H_2O adducts of the **$1\text{-}NH_2$** cluster (Fig. S1 and Table S3†). The ^1H NMR spectrum measured in acetone-d_6 exhibits two sets of resonances associated with the bt-NH_2 ligands in a $\sim 4:1$ ratio (Fig. S2†). Both sets of signals are shifted downfield with respect to the free ligand, consistent with ligand complexation in the Zn_5 cluster. The appearance of only two distinct ligand species is surprising given that the Zn_5 cluster can form several different isomers that differ in the relative orientations of the amine groups (Fig. S3†). However, the large number of adducts observed in the ESI-MS data suggests that rapid exchange of solvent ligands may influence the number of signals observed in the NMR spectrum. Notably, there is only one report of crystallographically characterized Zn_5 clusters containing monosubstituted benzotriazolate ligands.[57] These clusters exhibit C_1 symmetry with respect to the ligand orientations. Moreover, they were formed *in situ* during MOF assembly reactions and not characterized by NMR spectroscopy. Solubility tests reveal that **$1\text{-}NH_2$** is insoluble in water, slightly soluble in methanol and ethanol, and very soluble in polar aprotic solvents such as acetone, *N*-methylpyrrolidone (NMP), dimethyl sulfoxide (DMSO), and *N*,*N*-dimethylformamide (DMF). Attempts to obtain single crystals of **$1\text{-}NH_2$** for structural characterization were unsuccessful.

Solvothermal reaction of **$1\text{-}NH_2$** with dianhydrides PMDA, NDA, HFIPA, or BPDA in anhydrous NMP solvent at 200 °C results in imide condensation and formation of the corresponding **1-XDI** MOFs (Scheme 1). Solubility tests reveal that the solid products are insoluble in common organic solvents such as NMP, DMSO, DMF, *N*,*N*-dimethylacetamide (DMA), methanol, and ethanol, suggesting hyper-crosslinked structures. The powder X-ray diffraction (PXRD) patterns of **1-HFIPI**, **1-NDI** and **1-BPDI** are indicative of amorphous, aggregated structures, which is unsurprising given the variable connectivity and unsymmetric nature of the **$1\text{-}NH_2$** cluster (Fig. 1a). However, the PXRD pattern of **1-PMDI** exhibits several broad reflections in the $2\theta = 5–25°$ range, revealing the presence of a poorly crystalline phase. Importantly, these reflections do not match the crystalline phase of the H_2bbt-PMDI linker (Fig. S21†). The synthesis of **1-PMDI** is reproducible, and the PXRD patterns show the same crystalline phase over multiple batches (Fig. S5†). Unfortunately, the poor crystallinity and limited number of reflections in the PXRD pattern have hampered attempts to index the data and gain any further insight into the structure of the crystalline phase (see Part 4 in ESI† for more details).

The **1-XDI** MOFs proved amenable to acid digestion using methods developed for other Kuratowski cluster-based MOFs.[28,30] The digestion process cleaves the Zn-benzotriazolate bonds and solubilizes the ligand or linker fragments, which can then be identified and quantified by solution-state NMR analysis. The ^1H NMR spectra of the as-synthesized **1-XDI** products each exhibits a set of major

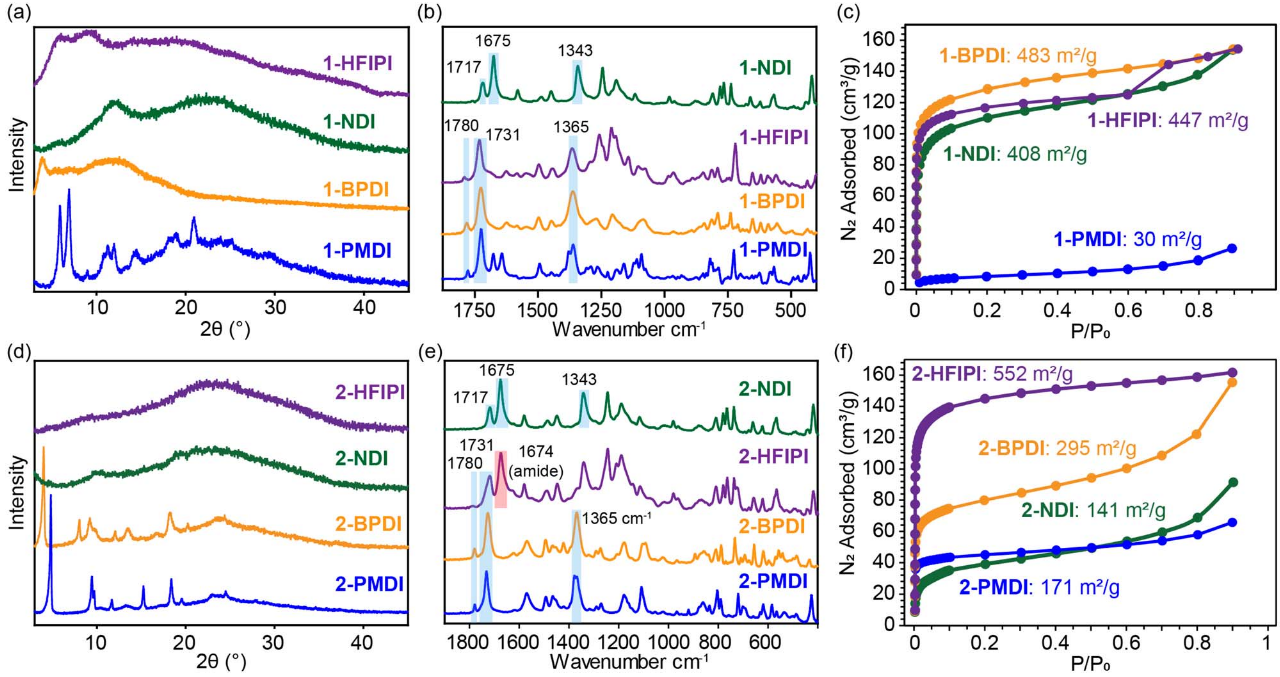

Fig. 1 (a) Overlay of PXRD patterns of **1-XDI** MOFs. (b) Overlay of ATR-IR spectra of **1-XDI** MOFs. Characteristic imide IR bands are highlighted in blue. (c) N_2 adsorption isotherms for **1-XDI** MOFs measured at 77 K. (d) Overlay of PXRD patterns of **2-XDI** MOFs. (e) Overlay of ATR-IR spectra of **2-XDI** MOFs. Characteristic imide IR bands are highlighted in blue. (f) N_2 adsorption isotherms for **2-XDI** MOFs measured at 77 K.

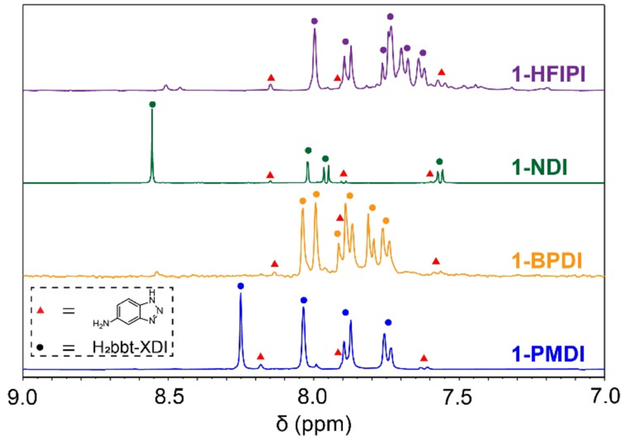

Fig. 2 Acid-digested ^1H NMR spectra of **1-XDI** MOFs. Peak assignments for H_2bbt-XDI and Hbt-NH_2 are labelled with coloured circles and red triangles, respectively.

aromatic resonances (Fig. 2) that match those observed for the authentic *bis*-imide ligands (Fig. S16–S19†). Remarkably, diimide condensation with the **1-NH₂** clusters appears to be nearly quantitative (>90%) and only small amounts of unreacted Hbt-NH_2 ligand are observed in the ^1H NMR spectra. The spectra also show some minor impurities that are attributed to incomplete imide condensation giving rise to amide/carboxylic acid species. In support of the NMR characterization, the ATR-IR spectra of **1-HFIPI**, **1-PMDI** and **1-BPDI** show the expected phthalic imide C═O symmetric and asymmetric stretching bands at 1731 and 1780 cm^{-1} (Fig. 1b). **1-NDI** also displays characteristic C═O symmetric and asymmetric stretching bands at lower energy (1717 cm^{-1} and 1675 cm^{-1}). Based on the ^1H NMR and ATR-IR data, the **1-XDI** MOFs exhibit a very high degree of imide connectivity between clusters. This result is somewhat unexpected given the amorphous nature of the samples. Nevertheless, the imide connections between neighboring **1-NH₂** clusters are likely facilitated by reversible amide formation at the high reaction temperature as well as the conformational flexibility of the amide intermediate. Dissociation of the benzotriazolate ligands from the **1-NH₂** cluster could also facilitate diimide linker condensation and MOF assembly. However, the benzotriazolate ligands are considerably inert owing to their μ₃-bridging mode, and to the best of our knowledge, there is no precedent for ligand exchange in Kuratowski cluster-based MOFs or molecular clusters. Further mechanistic studies will be necessary to better understand the assembly process, but the preceding data show that imide condensation provides a viable route to porous polymer networks with Kuratowski clusters.

Resonances associated with the presence of NMP guest molecules residing within the pores are also observed in the acid-digested ^1H NMR spectra of the as-synthesized **1-XDI** MOFs. The amount of NMP was determined by integration of the ^1H NMR spectra and closely matches the predicted solvent content from thermogravimetric analysis (TGA) (Fig. S6–S9†). The TGA data also show good thermal stability with the onset of thermal degradation ≥400 °C for all of the MOFs. The MOFs were solvent exchanged with methanol and subsequently desolvated by heating at 100 °C under high vacuum for 24 h. Acid-digested ^1H NMR analysis reveals some hydrolysis of the imide linkers, particularly for **1-BPDI** and **1-HFIPI**, as a result of the solvent exchange and thermal activation (Fig. S10–S13†). Combustion elemental analysis (C, H, N) and inductively coupled plasma atomic emission spectroscopy (ICP-OES, Zn) were carried out on the activated **1-XDI** MOFs (Tables S4–S7†). The results fit reasonably well to the empirical formulas expected for **1-NH$_2$** clusters connected by diimide linkers and show only modest deviations (<2.5 wt%) from the predicted compositions. N_2 adsorption isotherm measurements reveal BET surface areas of 30 m^2 g^{-1}, 447 m^2 g^{-1}, 408 m^2 g^{-1} and 483 m^2 g^{-1} for activated **1-PMDI**, **1-HFIPI**, **1-NDI** and **1-BPDI**, respectively (Fig. 1c). Some batch-to-batch variability was observed in the surface areas, but they remained reasonably consistent (Fig. S14†). Moreover, the surface areas of the **1-XDI** MOFs are comparable to, or even higher than, many reported porous organic polyimides and MCOFs (Tables S1 and S2†).[19–21,24] DFT pore size distributions calculated from the N_2 adsorption data show the presence of small micropores around 5–6 Å and a smaller volume fraction of micropores with ∼12 Å diameter (Fig. S15†). The relatively small micropores and the similarity in pore size distribution despite different linker lengths support the formation of highly disordered, crosslinked networks in the **1-XDI** MOFs.

Synthesis and characterization of 2-XDI MOFs

The predominantly amorphous nature of the **1-XDI** MOFs prompted us to investigate a coordinative assembly synthesis approach in hopes of obtaining crystalline analogues. *Bis*-benzotriazolate linkers (H_2bbt-XDI) were synthesized by condensation reactions between Hbt-NH$_2$ and the corresponding dianhydrides (Scheme 1). The new *bis*-imide compounds were characterized by CHN elemental analysis and ^{1}H NMR and ATR-IR spectroscopy (Fig. S16–S20†). The linkers were subsequently screened in solvothermal reactions with $ZnCl_2$ or $Zn(OAc)_2$ using DMF solvent and acid or base modulators (Table 1). Solid products were obtained for the solvothermal reactions of $Zn(OAc)_2$ with H_2bbt-PMDI and H_2bbt-BPDI. PXRD analysis of the corresponding materials, **2-PMDI** and **2-BPDI**, shows the presence of poorly crystalline phases that do not match those of the diimide linkers (Fig. 1d and S21, S22†). Unfortunately, we have thus far been unable to elucidate the structures of these products owing to their poor crystallinity and small crystallite size (see Part 4 in ESI†). Solvothermal reactions with H_2bbt-HFIPI and H_2bbt-NDI provided only clear solutions or amorphous solids under the screening conditions (Fig. S23 and S24†). The **2-XDI** syntheses, including those affording amorphous products, were scaled-up to generate **2-PMDI**, **2-BPDI**, **2-NDI** and **2-HFIPI**.

Table 1 Solvothermal screening conditions for synthesis of 2-XDI MOFs with H_2bbt-PMDI, H_2bbt-NDI, H_2bbt-BPDI, H_2bbt-HFIPI

Condition number (*n*)	Metal salt	Modulator
1	$Zn(OAc)_2$	Acetic acid
2	$Zn(OAc)_2$	None
3	$Zn(OAc)_2$	Triethylamine
4	$ZnCl_2$	Acetic acid
5	$ZnCl_2$	None
6	$ZnCl_2$	Triethylamine

TGA analysis of the **2-XDI** products after desolvation under high vacuum at 100 °C for 24 h reveals that they are generally less stable than the **1-XDI** analogues with the onset of thermal degradation increasing in the order **2-NDI** (310 °C) < **2-BPDI** (350 °C) < **2-PMDI** (390 °C) < **2-HFIPI** (400 °C) (Fig. S25–S28†). Small mass losses of 2–6 wt% are observed below 100 °C and attributed to a small amount of water adsorbed upon exposure to ambient conditions. N_2 adsorption isotherms (77 K) measured after desolvation show modest porosity with calculated BET surface areas of 171, 295, 141, and 552 m^2 g^{-1} for **2-PMDI**, **2-BPDI**, **2-NDI** and **2-HFIPI**, respectively (Fig. 1f). The DFT pore size distributions are similar to those observed for the **1-XDI** MOFs and indicate the presence two types of micropores that are 5–6 Å and ∼12 Å in diameter (Fig. S29†). Notably, **2-PMDI** exhibits increased porosity compared to **1-PDMI**, consistent with structural differences reflected in the PXRD patterns.

A combination of acid-digested ^{1}H NMR analysis, ATR-IR spectroscopy, CHN elemental analysis, and ICP-OES have been used to gain insight into the composition of the **2-XDI** MOFs. The acid-digested ^{1}H NMR spectra for **2-PMDI**, **2-BPDI**, and **2-NDI** confirm the presence of intact [bbt-XDI]$^{2-}$ linkers (Fig. S30–S32†). However, **2-HFIPI** shows a complex mixture of amide species resulting from hydrolysis of the imide linkers during the solvothermal reaction (Fig. S33†). This conclusion is supported by the ATR-IR spectra of the **2-XDI** MOFs (Fig. 1e). **2-PMDI** and **2-BPDI** exhibit intense features at 1731 and 1780 cm^{-1} that correspond to phthalimide C═O symmetric and asymmetric stretching bands. The six-membered imide ring in **2-NDI** displays characteristic C═O symmetric and asymmetric stretching bands at lower energy (1717 cm^{-1} and 1675 cm^{-1}). Bands corresponding to a C–N–C stretching mode and out of plane bending of the imide ring are also observed at 1365 and 738 cm^{-1}, respectively. On the other hand, the ATR-IR spectrum for **2-HFIPI** shows an intense C═O stretch at 1674 cm^{-1} that can be attributed to amide species arising from hydrolysis of the H_2bbt-HFIPI linker.

Since the **2-XDI** MOFs were prepared from Zn^{2+} salts *via* coordination assembly and the structures could not be determined using X-ray or electron diffraction, the identity of the metal building units remains ambiguous. The elemental analysis data show significant deviations from the C, H, N, and Zn mass percent compositions expected for the presence of Zn_5 clusters derived from **1-NH$_2$** (Tables S8–S11†). Moreover, the deviations for the **2-XDI** MOFs are considerably larger than those observed for the **1-XDI** series, and there is no clear trend indicating the **2-XDI** materials have a consistent metal:linker stoichiometry among the series. Based on literature precedent, other metal building units such as Zn_9 clusters or infinite chains may also form during solvothermal assembly.[32,48–54,58,59] This leaves open the possibility that the materials are assembled from a less commonly observed SBU.

Gas adsorption properties of 1-XDI and 2-XDI MOFs

CO_2, C_2H_2, C_2H_4, C_2H_6, C_3H_6, and C_3H_8 gas adsorption isotherms (300 K) were measured for the activated **1-XDI** and **2-XDI** MOFs to investigate their potential for selective CO_2/C_2H_2, C_2H_4/C_2H_6, and C_3H_6/C_3H_8 adsorptive separation processes. From these data, the corresponding ideal adsorbed solution theory (IAST) selectivity values have been calculated for binary, equimolar gas mixtures at 1 bar and 300 K (Tables S13 and S14†). Consistent with their relatively low surface areas, the **1-XDI** and **2-XDI** materials all exhibit gas adsorption capacities of less than 2 mmol g^{-1} at 1 bar (Tables S15 and S16†). With the exception of **1-PMDI**, the gas uptake profiles and capacities of the **1-XDI** MOFs are nearly identical across all tested gases (Fig. 3 and S38†). This behavior is consistent with their similar pore size distributions and comparable BET surface areas (Fig. 1c and S15†). **1-PMDI** exhibits negligible adsorption of all of the gases studied, which is in accordance with its non-porous structure. The remaining **1-XDI** MOFs exhibit favorable adsorption of C_2H_2 over CO_2 with modest IAST selectivities in the 2.3–2.9 range but show little to no selectivity for C_2H_4/C_2H_6 or C_3H_6/C_3H_8 separation (Fig. 3).

The **2-XDI** materials exhibit more variability in their gas adsorption profiles with similar or slightly lower capacities than the **1-XDI** analogues (Fig. 4 and S39†). They also show modest IAST selectivity values (2.3–3.4) for adsorption of C_2H_2 over CO_2. Despite its low surface area (171 m^2 g^{-1}), crystalline **2-PMDI** has the steepest C_2H_2 uptake profile among the series. For the larger C_2 and C_3 gases, the order of gas uptake at 1 bar follows the trend suggested by the BET surface areas: **2-HFIPI** > **2-BPDI** > **2-**

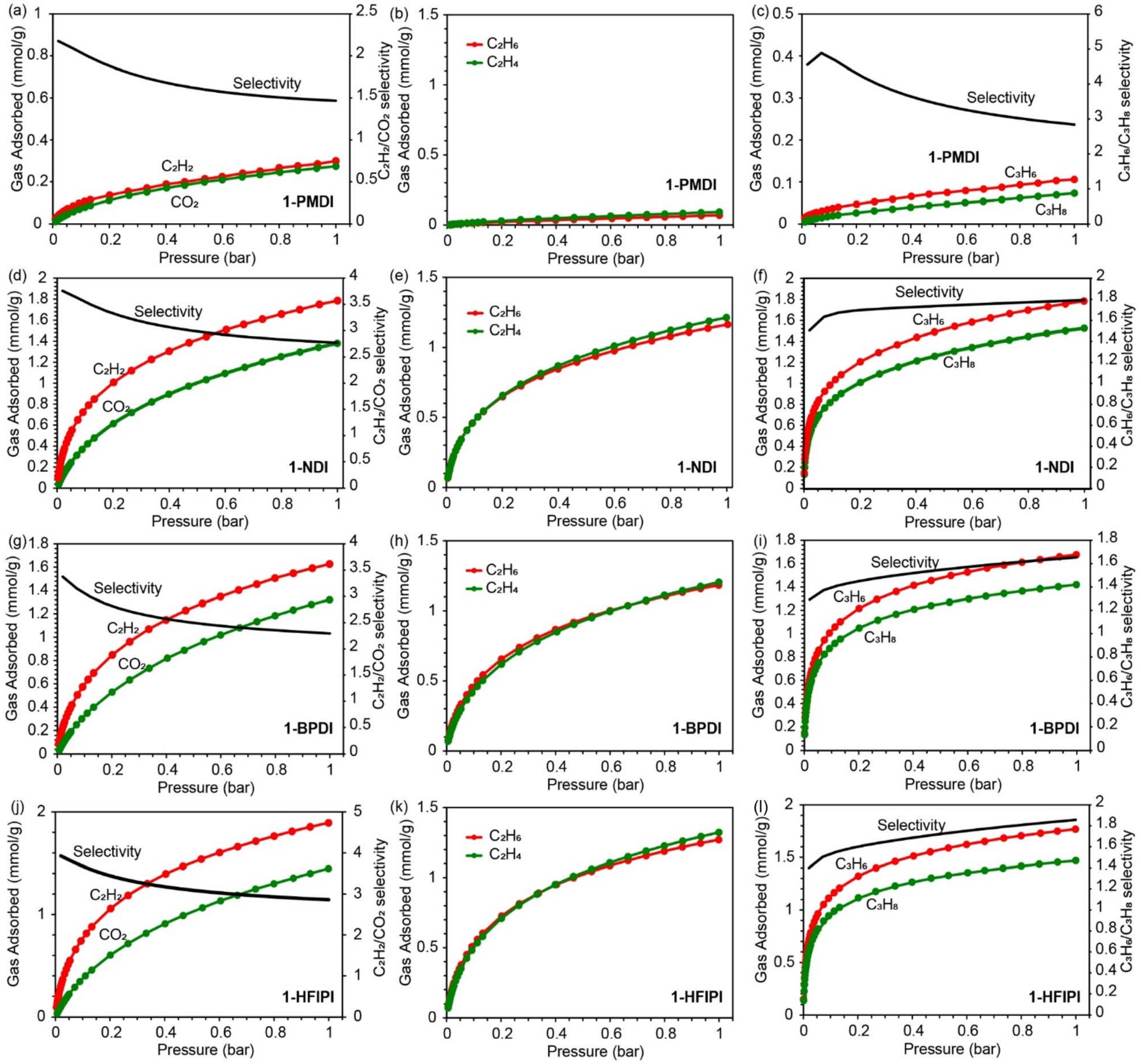

Fig. 3 (a)–(l) C_2H_2 and CO_2, C_2H_4 and C_2H_6, C_3H_6 and C_3H_8 adsorption isotherms (left y-axis) and predicted IAST selectivity at 300 K (right y-axis) for **1-XDI** MOFs.

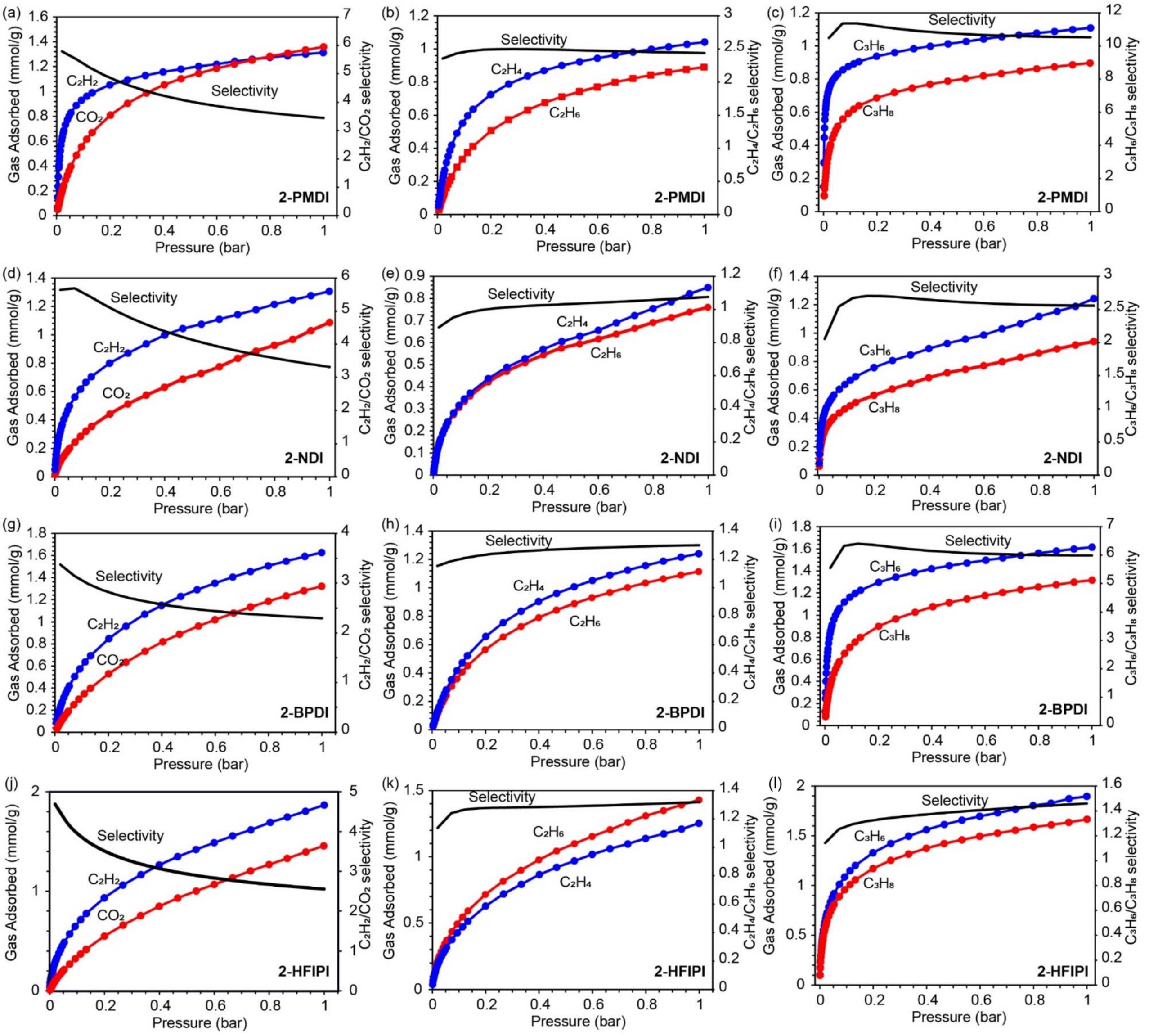

Fig. 4 (a)–(l) C_2H_2 and CO_2, C_2H_4 and C_2H_6, C_3H_6 and C_3H_8 adsorption isotherms (left *y*-axis) and predicted IAST selectivity at 300 K (right *y*-axis) for **2-XDI** MOFs.

PMDI > **2-NDI**. No significant selectivity is observed for C_2H_4/C_2H_6 adsorption, but all of the **2-XDI** materials show some selectivity for adsorption of C_3H_6 over C_3H_8. In particular, **2-PMDI** and **2-BPDI** show high calculated IAST selectivity values of 10 and 6, respectively, up to 1 bar total pressure (Fig. 4). This selectivity is comparable to other porous materials reported for C_3H_6/C_3H_8 separation, including AGTU-3a (7.0),[60] MAF-23-O (8.8),[61] Ni-NP (10.5),[62] and Ni-MOF-74 (10).[63] However, these selectivities are much lower than those of state-of-the-art materials such as Co-gallate (333) and UTSA-400 (>10^7) (Table S17†).[64,65]

Despite their amorphous or poorly crystalline structures, the **1-XDI** and **2-XDI** materials both show selective C_2H_2 adsorption with similar C_2H_2/CO_2 capacities and IAST selectivity values in the 2.3–3.4 range. While neither are on par with the top-performing materials for C_2H_2/CO_2 separation, they are comparable to CAU-10H (2.5),[66] [Ni(tzba)$_{0.5}$(F)(bpy)] (2.2),[67] [Ca(dtztp)$_{0.5}$] (1.7),[68] and NUM-14a (3.3) (Table S18†).[69] The most striking difference in adsorption properties between the **1-XDI** and **2-XDI** series is the relatively high C_3H_6/C_3H_8 selectivity of **2-PMDI** and **2-BPDI**. Although the origin of this difference remains unclear, it is notable that these are the only members of the two series that are both crystalline and porous. In this regard, crystalline frameworks resulting from the traditional MOF solvothermal synthesis route appear to offer some advantages toward adsorbent design for gas separation.

Conclusions

In summary, four novel **1-XDI** MOFs have been prepared by condensation of amine-functionalized Kuratowski clusters (**1-NH$_2$**) with organic dianhydrides. To the best of our knowledge, this work represents the first example of incorporation of Kuratowski clusters into porous coordination polymers using a condensation assembly approach. The properties of these new materials have been compared to **2-XDI** analogues synthesized by a solvothermal coordinative assembly route commonly used for MOFs. Unsurprisingly, the two different synthetic approaches do not converge to afford analogous materials. The **2-XDI** MOFs differ from the **1-XDI** MOFs in terms of structure, composition, and gas adsorption properties. Crystalline phases were obtained for **1-PMDI**, **2-PMDI**, and **2-BPDI**, and PXRD data indicate that **1-PMDI** and **2-PMDI** adopt different framework structures. Despite extensive synthetic screening, neither route gives highly crystalline materials amenable to complete structural characterization *via* X-ray or electron diffraction. Based on acid-digested ^{1}H NMR spectra, the **1-XDI** and **2-XDI** MOFs contain intact [bbt-XDI]$^{2-}$ linker species. Remarkably, the ^{1}H NMR spectra show nearly complete conversion to diimide species in the as-synthesized **1-XDI** MOFs with only small amounts of unreacted bt-NH$_2$ groups and amide/carboxylate species.

The BET surface areas of the **1-XDI** MOFs are all modest and quite consistent, with the exception of **1-PMDI** which is essentially nonporous. The **2-XDI** MOFs show greater variability in their N_2 uptake, and generally exhibit lower BET surface areas than the **1-XDI** analogues. Single component gas adsorption isotherms with CO_2, C_2H_2, C_2H_4, C_2H_6, C_3H_6, and C_3H_8 were also measured for the **1-XDI** and **2-XDI** MOFs. All of the materials studied showed modest IAST selectivities (2.3–3.4) for adsorption of C_2H_2 from C_2H_2/CO_2 binary gas mixtures. In addition, **2-PMDI** and **2-BPDI** exhibit good selectivity towards C_3H_6/C_3H_8 separation, but similar behavior was not observed for the **1-PMDI** and **1-BPDI** MOFs.

Overall, the results of this study demonstrate that imide condensation reactions can be used to prepare porous MOFs from amine-functionalized metal clusters with a high degree of connectivity. This approach is complementary to traditional MOF solvothermal synthesis which takes place exclusively *via* coordinative bond formation and yields materials with different compositions and properties. Condensation assembly of MOFs opens up new possibilities for the introduction of diverse functionalities for gas separation and other applications.

Experimental section

General considerations

1*H*-Benzo[*d*][1,2,3]triazol-5-amine (Hbt-NH$_2$) was synthesized from 4-nitro-1,2-phenylenediamine according to report procedures.[70] Pyromellitic dianhydride (PMDA), naphthalenetetracarboxylic dianhydride (NDA), 3,3′,4,4′-biphenyltetracarboxylic dianhydride (BPDA), 4,4′-(hexafluoroisopropylidene)diphthalic anhydride (HFIPA) and 4-nitro-1,2-phenylenediamine were purchased from Tokyo Chemical Industry Co., Ltd. $Zn(OAc)_2 \cdot 2H_2O$ (Alfa Aesar), $ZnCl_2$ (98.0% Fisher Scientific), *N*,*N*-dimethylformamide (DMF, Fisher), Triethylamine (Fisher, 99.9%), sodium nitrite, 10 wt% Pd on carbon, hydrazine and glacial acetic acid (Fisher) were used as received. *N*-Methyl pyrrolidone (NMP, 99%, Honeywell) was dried by distillation from calcium hydride. All other solvents and reagents were of reagent grade and used as received. Routine powder X-ray diffraction patterns for phase identification were collected using a Rigaku Miniflex 600 diffractometer with nickel-filtered Cu-Kα radiation ($\lambda = 1.5418$ Å). ESI mass spectroscopic data were collected with a Bruker Impact II QqTOF Mass Spectrometer. ATR-IR spectra were measured using a Bruker Alpha II spectrometer with a diamond ATR accessory. Solution-state NMR spectra were measured using a Bruker DPX 400 or 600 MHz spectrometer. For ^{1}H NMR spectra, the solvent resonance was used as an internal chemical shift reference. MOF samples were digested for solution-state ^{1}H NMR analysis by suspending 15–20 mg of solid in CF_3CO_2H (0.1 mL) and gently heating the suspensions until all of the solids dissolved. Dimethyl sulfoxide (DMSO-d_6, 1 mL) was then added to the solutions to provide a lock signal for shimming. Solvent-suppressed ^{1}H NMR spectra were collected using a 180° water selective excitation sculpting with default parameters and pulse shapes. Briefly, spectra were collected using selective pulses of 1 ms with the transmitter frequency set to the center of the solvent resonance. The recycle delay between scans was 2 s, 16 K points were collected, and the acquisition time was 0.7 s. Elemental microanalyses (C, H, N) and inductively coupled plasma atomic emission spectroscopy (Zn) were performed by Robertson Microlit Laboratories, Ledgewood, NJ.

Gas adsorption isotherm measurements

Single-component gas adsorption isotherms were measured using a Micromeritics 3Flex Surface Characterization Analyzer. All measurements were performed using the highest purity gases available from Linde or Praxair (N_2, NI 5.0UH-K; CO_2, CD 5.0LS-K; CO_2, CD 5.0LS-K; C_2H_2, AC 2.6AA; C_2H_4, EY 5.0RS-K; C_2H_6, ET 5.0RS-G; C_3H_6, PY 2.5IS-PX; C_3H_8, PR 2.5ISK). Prior to analysis, samples (100–200 mg) were transferred to oven-dried and tared sample tubes equipped with TranSeals (Micromeritics) and heated to 100 °C (1 °C min^{-1}) under vacuum until the outgassing rate was less than 0.0033 mbar min^{-1}. BET surface areas were calculated from the N_2 adsorption isotherms (77 K) by fitting the data to the BET equation with the appropriate pressure range ($0.0001 \leq P/P_o \leq 0.1$) determined by the consistency criteria of Rouquerol.[71,72] An open-source Python-based code package PyGAPS (Python General Adsorption Processing Suite) was used for isotherm fitting and the calculation of spreading pressure to generate IAST selectivity values at different pressures.[73]

Synthesis of H$_2$-bbtXDI linkers

H$_2$bbt-PMDI. PMDA (320 mg, 1.5 mmol, 1 equiv.) and Hbt-NH$_2$ (400 mg, 3.0 mmol, 2 equiv.) were suspended in anhydrous DMF (1.5 mL) in 10 mL Schlenk flask under an N_2 atmosphere. The flask was fit with a reflux condenser and heated to reflux for 12 hours. The product precipitated upon cooling to room temperature, was collected by filtration, and washed with DMF (5 × 10 mL) and MeOH (5 × 10 mL). Yield: 540 mg, 80%. ^{1}H NMR (DMSO-d$_6$, 600 MHz), δ (ppm): 8.24 (s, 2H, Ar–H), 8.04 (s, 2H, Ar–H), 7.89 (d, 2H, Ar–H, $^3J_{H-H} = 6$ Hz), 7.74 (d, 2H, Ar–H,

$^3J_{H-H}$ = 6 Hz). Anal. Calcd for $C_{22}H_{10}N_8O_4$: C, 58.67; H, 2.24; N, 24.88; found: C, 58.62; H, 2.17; N, 24.79.

H_2bbt-NDI. NDA (250 mg, 0.93 mmol, 1 equiv.) and Hbt-NH_2 (250 mg, 1.86 mmol, 2 equiv.) were suspended in anhydrous DMF (6 mL) in a 10 mL Schlenk flask under an N_2 atmosphere. The flask was fit with a reflux condenser and heated to reflux for 12 hours. The product precipitated upon cooling to room temperature, was collected by filtration, and washed with DMF (5 × 10 mL) and MeOH (5 × 10 mL). Yield: 260 mg, 56%. ^{1}H NMR (DMSO-d_6, 400 MHz), δ (ppm): 8.56 (s, 4H, Ar–H), 8.01 (s, 2H, Ar–H), 7.95 (d, 2H, Ar–H, $^3J_{H-H}$ = 10 Hz), 7.56 (d, 2H, Ar–H, $^3J_{H-H}$ = 10 Hz). Anal. Calcd for $C_{26}H_{12}N_8O_4$: C, 62.40; H, 2.42; N, 22.39; found: C, 61.79; H, 2.43; N, 22.39.

H_2bbt-BPDI·0.15 DMF. BPDA (439 mg, 1.5 mmol, 1 equiv.) was suspended in anhydrous DMF (1 mL) in a 10 mL Schlenk flask under an N_2 atmosphere. The suspension was heated to 150 °C in a sand bath with stirring until the dianhydride was fully dissolved. A solution of Hbt-NH_2 (400 mg, 3.0 mmol, 2 equiv.) dissolved in DMF (1.5 mL) was then added dropwise to the hot solution. The reaction flask was fit with a reflux condenser, heated at 150 °C for 5 hours, and then heated to reflux for 12 hours. The product precipitated upon cooling to room temperature, was collected by filtration, and washed with DMF (3 × 50 mL) and MeOH (3 × 50 mL). Yield: 549 mg, 70%. ^{1}H NMR (DMSO-d_6, 400 MHz), δ (ppm): 8.04 (s, 1H, Ar–H), 7.99 (s, 2H, Ar–H), 7.91 (d, 2H, Ar–H, $^3J_{H-H}$ = 12 Hz), 7.88 (d, 2H, Ar–H, $^3J_{H-H}$ = 8 Hz). 7.80 (d, 2H, Ar–H, $^3J_{H-H}$ = 8 Hz), 7.75 (d, 2H, Ar–H, $^3J_{H-H}$ = 8 Hz). The ^{1}H NMR spectrum indicates that product retains a small amount of DMF (~0.15 equiv.) even after drying. The residual solvent has been accounted for in the elemental analysis data. Anal. Calcd for $C_{28.75}H_{13.35}N_{8.15}O_{4.15}$: C, 62.54; H, 2.62; N, 20.84; found: C, 62.68; H, 2.51; N, 20.44.

H_2bbt-HFIPI. HFIPA (497 mg, 1.12 mmol, 1 equiv.) and Hbt-NH_2 (300 mg, 2.24 mmol, 2 equiv.) were suspended in acetic acid (1.5 mL) in a 10 mL Schlenk flask under an N_2 atmosphere. The reaction flask was fit with a reflux condenser and heated to reflux for 12 hours. The product precipitated upon cooling to room temperature, was collected by filtration, and washed with methanol (10 × 10 mL). Yield: 620 mg, 82%. ^{1}H NMR (DMSO-d_6, 600 MHz), δ (ppm): 15.94 (s, 2H, N–H), 8.23 (d, 2H, Ar–H, $^3J_{H-H}$ = 8 Hz), 8.20 (br, 1H, Ar–H), 8.16 (br, 1H, Ar–H) 8.01 (d, 2H, Ar–H, $^3J_{H-H}$ = 10 Hz), 7.92 (br, 2H, Ar–H), 7.78 (s, 2H, Ar–H), 7.60 (br, 1H, Ar–H), 7.48 (br, 1H, Ar–H). Anal. Calcd for $C_{31}H_{14}F_6N_8O_4$: C, 55.04; H, 2.09; N, 16.56; found: C, 54.30; H, 1.97; N, 16.33.

Synthesis of 1-NH_2 (Zn_5Cl_4(bt-NH_2)$_6$)

Hbt-NH_2 (1.25 g, 9.30 mmol, 6 equiv.) was dissolved in ethanol (50 mL) in a 250 mL round bottom flask. A solution of anhydrous $ZnCl_2$ (1.06 g, 7.8 mmol, 5 equiv.) and 2,6-lutidine (0.997 g, 9.30 mmol, 6 equiv.) in ethanol (20 mL) was added dropwise with stirring. The resulting mixture was heated to reflux for 1 h resulting in precipitation of a light-yellow solid. The solid was collected by filtration, washed with hot ethanol, and dried overnight *in vacuo* at 100 °C to afford the product (1.23 g, 62%). ^{1}H NMR (acetone-d_6, 400 MHz) δ (ppm): 8.41 (dd, 1H, Ar–H, $^3J_{H-H}$ = 9 Hz), 8.18 (q, 4H, Ar–H, $^3J_{H-H}$ = 9 Hz), 7.66 (t, 1H, Ar–H, $^3J_{H-H}$ = 11 Hz), 7.39 (t, 4H, Ar–H, $^3J_{H-H}$ = 11 Hz), 7.17 (d, 4H, Ar–H, $^3J_{H-H}$ = 7 Hz), 7.09 (d, 1H, Ar–H, $^3J_{H-H}$ = 8 Hz), 5.39 (br, 8H, –NH_2). See Fig. S1 and Table S3 in the ESI† for ESI-MS data.

General procedure for 1-XDI MOF synthesis

The **1-XDI** MOFs were synthesized by solvothermal reaction of **1-NH_2** (1 equiv., 6 amine groups per cluster) with the corresponding dianhydride (3 equiv.) (Scheme 1). Under an N_2 atmosphere, a pre-dried Schlenk flask was charged with XDA (XDA = PMDA, NDA, BPDA, HFIPA; 3 equiv., specific quantities given below) and anhydrous NMP (half of the total solvent amount given below) and fit with a vented addition funnel. The mixture was heated to 200 °C in a sand bath with stirring, and a solution of **1-NH_2** (1 equiv., specific quantities given below) in NMP was added dropwise to the XDA solution over the course of 4 h *via* the pre-dried addition funnel. The addition funnel was quickly replaced with a glass stopper, and the reaction was heated at 200 °C for 24 hours under an N_2 atmosphere. Upon cooling to room temperature, the resulting precipitate was isolated by filtration. The solid product was immersed in fresh NMP (100 mL) and heated at 120 °C for 24 hours to remove any trapped XDA. The solid was collected by filtration, washed with additional NMP (3 × 50 mL) and MeOH (3 × 50 mL). The product was dried *in vacuo* at 100 °C for 24 hours prior to gas adsorption isotherm measurements.

1-PMDI. 800 mg **1-NH_2**, 413 mg PMDA, and 30 mL of NMP were used. Yield: 1.12 g. Anal. Calcd for $Zn_5Cl_4(C_{22}H_8N_8O_4)_3$: C, 43.70; H, 1.33; N, 18.53; Zn, 18.03; found: C, 45.95; H, 1.74; N, 19.56; Zn, 19.41.

1-NDI. 400 mg **1-NH_2**, 254 mg NDA, and 6 mL of NMP were used. Yield: 590 mg. Anal. Calcd for $Zn_5Cl_4(C_{26}H_{10}N_8O_4)_3$: C, 54.14; H, 2.05; N, 16.29; found: C, 54.30; H, 1.97; N, 16.33.

1-BPDI. 400 mg **1-NH_2**, 279 mg BPDA, and 16 mL of NMP were used. Yield: 650 mg. Anal. Calcd for $Zn_5Cl_4(C_{28}H_{12}N_8O_4)_3$: C, 49.40; H, 1.78; N, 16.46; Zn, 16.01. Found: C, 50.51; H, 2.21; N, 16.51; Zn, 14.01.

1-HFIPI. 500 mg **1-NH_2**, 526 mg HFIPA, and 13 mL of NMP were used. Yield: 970 mg. Anal. Calcd for $Zn_5Cl_4(C_{31}H_{12}F_6N_8O_4)_3$: C, 44.82; H, 1.46; N, 13.49; Zn, 13.12. Found: C, 45.88; H, 1.66; N, 13.25; Zn, 13.43.

General procedure for 2-XDI MOF synthetic screening

H_2bbt-XDI linker (10 mg, 1 equiv.) and modulator (0.2 mL) were mixed with DMF (3 mL) in a 20 mL scintillation vial, and the suspension was sonicated to ensure maximum dissolution of the linker. The corresponding Zn source (4 equiv.) was added, and the vial was sealed with a Teflon-lined cap (Qorpak, #272628). The reaction vial was then placed in a room temperature, programmable oven and heated to 120 °C for 24 hours. Upon cooling to room temperature, the resulting solids were collected by filtration and washed with DMF (3 × 10 mL) and methanol (3 × 10 mL). The products are labeled according to the screening condition number (n) in Table 1 (*i.e.* **2-XDI-*n***; XDI = PMDI, NDI, BPDI and HFIPI; n = 1, 2, 3, 4, 5, 6;).

Scale-up synthesis of 2-XDI MOFs

The **2-XDI** MOF syntheses were scaled up (120 mg of linker) according to the results of PXRD analysis from the screening reactions (Fig. S21–S24†). Based on these data, **2-PMDI-1**, **2-NDI-5**, **2-BPDI-1**, and **2-HFIPI-5** were chosen for synthetic scale-up. A 100 mL screw top media jar was used as the reaction vessel.

2-PMDI. Yield: 170 mg. Anal. Found: C, 43.16; H, 2.24; N, 15.66.

2-NDI. Yield: 45 mg. Anal. Found: C, 50.08; H, 2.19; N, 17.77; Zn, 13.82.

2-BPDI. Yield: 120 mg. Anal. Found: C, 48.98; H, 2.72; N, 14.95; Zn, 16.40.

2-HFIPI. Yield: 25 mg. Anal. Found: C, 45.40; H, 1.94; N, 13.70; Zn, 12.98.

Data availability

The data supporting this article have been included as part of the ESI.†

Author contributions

Q. L.: conceptualization, investigation, formal analysis, writing; J. S. H.: investigation; Z. C.: investigation; C. R. W.: conceptualization, formal analysis, supervision, writing.

Conflicts of interest

There are no conflicts to declare.

Acknowledgements

This work was supported by an Early Career Faculty grant (80NSSC18K1504) from NASA's Space Technology Research Grants Program. We thank Chandler Greenwell, Xuetao Liu and XtalPi, Inc. for performing micro-crystal electron diffraction experiments.

References

1 J. R. Li, R. J. Kuppler and H. C. Zhou, *Chem. Soc. Rev.*, 2009, **38**, 1477–1504.
2 J. Liang, Y.-B. Huang and R. Cao, *Coord. Chem. Rev.*, 2019, **378**, 32–65.
3 R.-B. Lin, S. Xiang, W. Zhou and B. Chen, *Chem*, 2020, **6**, 337–363.
4 J. Lee, O. K. Farha, J. Roberts, K. A. Scheidt, S. T. Nguyen and J. T. Hupp, *Chem. Soc. Rev.*, 2009, **38**, 1450–1459.
5 Q. Wang and D. Astruc, *Chem. Rev.*, 2020, **120**, 1438–1511.
6 H. Bin Wu and X. W. Lou, *Sci. Adv.*, 2017, **3**, eaap9252.
7 J. Ren, Y. Huang, H. Zhu, B. Zhang, H. Zhu, S. Shen, G. Tan, F. Wu, H. He, S. Lan, X. Xia and Q. Liu, *Carbon Energy*, 2020, **2**, 176–202.
8 S. R. Batten, N. R. Champness, X.-M. Chen, J. Garcia-Martinez, S. Kitagawa, L. Öhrström, M. O'Keeffe, M. Paik Suh and J. Reedijk, *Pure Appl. Chem.*, 2013, **85**, 1715–1724.
9 T. D. Bennett and S. Horike, *Nat. Rev. Mater.*, 2018, **3**, 431–440.
10 Z. Yu, L. Tang, N. Ma, S. Horike and W. Chen, *Coord. Chem. Rev.*, 2022, **469**, 214646.
11 N. Ma and S. Horike, *Chem. Rev.*, 2022, **122**, 4163–4203.
12 Z. Lin, J. J. Richardson, J. Zhou and F. Caruso, *Nat. Rev. Chem*, 2023, **7**, 273–286.
13 K. Geng, T. He, R. Liu, S. Dalapati, K. T. Tan, Z. Li, S. Tao, Y. Gong, Q. Jiang and D. Jiang, *Chem. Rev.*, 2020, **120**, 8814–8933.
14 F. Haase and B. V Lotsch, *Chem. Soc. Rev.*, 2020, **49**, 8469–8500.
15 S. Das, P. Heasman, T. Ben and S. Qiu, *Chem. Rev.*, 2017, **117**, 1515–1563.
16 O. M. Yaghi, M. J. Kalmutzki and C. S. Diercks, in *Introduction to Reticular Chemistry*, 2019, pp. 177–195.
17 J. Dong, X. Han, Y. Liu, H. Li and Y. Cui, *Angew. Chem., Int. Ed.*, 2020, **59**, 13722–13733.
18 H. L. Nguyen, F. Gándara, H. Furukawa, T. L. H. Doan, K. E. Cordova and O. M. Yaghi, *J. Am. Chem. Soc.*, 2016, **138**, 4330–4333.
19 S. K. Elsaidi, M. H. Mohamed, J. S. Loring, B. P. McGrail and P. K. Thallapally, *ACS Appl. Mater. Interfaces*, 2016, **8**, 28424–28427.
20 R. Jangir, A. C. Kalita, D. Kaleeswaran, S. K. Gupta and R. Murugavel, *Chem.–Eur. J.*, 2018, **24**, 6178–6190.
21 W. Rong-Jia, Z. Hou-Gan, Z. Zhi-Yin, N. Guo-Hong and L. Dan, *CCS Chem.*, 2020, **3**, 2045–2053.
22 H.-S. Lu, W.-K. Han, X. Yan, C.-J. Chen, T. Niu and Z.-G. Gu, *Angew. Chem., Int. Ed.*, 2021, **60**, 17881–17886.
23 X. Li, J. Wang, F. Xue, Y. Wu, H. Xu, T. Yi and Q. Li, *Angew. Chem., Int. Ed.*, 2021, **60**, 2534–2540.
24 H.-G. Zhou, R.-Q. Xia, J. Zheng, D. Yuan, G.-H. Ning and D. Li, *Chem. Sci.*, 2021, **12**, 6280–6286.
25 W.-K. Han, Y. Liu, X. Yan, Y. Jiang, J. Zhang and Z.-G. Gu, *Angew. Chem., Int. Ed.*, 2022, **61**, e202208791.
26 L. Sun, M. Lu, Z. Yang, Z. Yu, X. Su, Y.-Q. Lan and L. Chen, *Angew. Chem., Int. Ed.*, 2022, **61**, e202204326.
27 R.-J. Wei, P.-Y. You, H. Duan, M. Xie, R.-Q. Xia, X. Chen, X. Zhao, G.-H. Ning, A. I. Cooper and D. Li, *J. Am. Chem. Soc.*, 2022, **144**, 17487–17495.
28 C. E. Bien, K. K. Chen, S. C. Chien, B. R. Reiner, L. C. Lin, C. R. Wade and W. S. W. Ho, *J. Am. Chem. Soc.*, 2018, **140**, 12662–12666.
29 A. M. Wright, Z. Wu, G. Zhang, J. L. Mancuso, R. J. Comito, R. W. Day, C. H. Hendon, J. T. Miller and M. Dincă, *Chem*, 2018, **4**, 2894–2901.
30 C. E. Bien, Q. Liu and C. R. Wade, *Chem. Mater.*, 2020, **32**, 489–497.
31 Z. Cai, C. E. Bien, Q. Liu and C. R. Wade, *Chem. Mater.*, 2020, **32**, 4257–4264.
32 Q. Liu, N. Hoefer, G. Berkbigler, Z. Cui, T. Liu, A. C. Co, D. W. McComb and C. R. Wade, *Inorg. Chem.*, 2022, **61**, 18710–18718.
33 J. Teufel, H. Oh, M. Hirscher, M. Wahiduzzaman, L. Zhechkov, A. Kuc, T. Heine, D. Denysenko and D. Volkmer, *Adv. Mater.*, 2013, **25**, 635–639.

34 M. H. Mohamed, Y. Yang, L. Li, S. Zhang, J. P. Ruffley, A. G. Jarvi, S. Saxena, G. Veser, J. K. Johnson and N. L. Rosi, *J. Am. Chem. Soc.*, 2019, **141**, 13003–13007.

35 Q. Liu, S. G. Cho, J. Hilliard, T.-Y. Wang, S.-C. Chien, L.-C. Lin, A. C. Co and C. R. Wade, *Angew. Chem., Int. Ed.*, 2023, **62**, e202218854.

36 E. D. Metzger, C. K. Brozek, R. J. Comito and M. Dincă, *ACS Cent. Sci.*, 2016, **2**, 148–153.

37 R. J. Comito, K. J. Fritzsching, B. J. Sundell, K. Schmidt-Rohr and M. Dincă, *J. Am. Chem. Soc.*, 2016, **138**, 10232–10237.

38 E. D. Metzger, R. J. Comito, C. H. Hendon and M. Dincă, *J. Am. Chem. Soc.*, 2017, **139**, 757–762.

39 R. J. Comito, Z. Wu, G. Zhang, J. A. Lawrence III, M. D. Korzyński, J. A. Kehl, J. T. Miller and M. Dincă, *Angew. Chem., Int. Ed.*, 2018, **57**, 8135–8139.

40 E. D. Metzger, R. J. Comito, Z. Wu, G. Zhang, R. C. Dubey, W. Xu, J. T. Miller and M. Dincă, *ACS Sustain. Chem. Eng.*, 2019, **7**, 6654–6661.

41 H. D. Park, R. J. Comito, Z. Wu, G. Zhang, N. Ricke, C. Sun, T. Van Voorhis, J. T. Miller, Y. Román-Leshkov and M. Dincă, *ACS Catal.*, 2020, **10**, 3864–3870.

42 D. Denysenko, M. Grzywa, J. Jelic, K. Reuter and D. Volkmer, *Angew. Chem., Int. Ed.*, 2014, **53**, 5832–5836.

43 A. M. Wright, A. J. Rieth, S. Yang, E. N. Wang and M. Dincă, *Chem. Sci.*, 2018, **9**, 3856–3859.

44 R. Röß-Ohlenroth, B. Bredenkötter and D. Volkmer, *Organometallics*, 2019, **38**, 3444–3452.

45 L. Li, Y. Yang, M. H. Mohamed, S. Zhang, G. Veser, N. L. Rosi and J. K. Johnson, *Organometallics*, 2019, **38**, 3453–3459.

46 G. M. Su, H. Wang, B. R. Barnett, J. R. Long, D. Prendergast and W. S. Drisdell, *Chem. Sci.*, 2021, **12**, 2156–2164.

47 B. R. Barnett, H. A. Evans, G. M. Su, H. Z. H. Jiang, R. Chakraborty, D. Banyeretse, T. J. Hartman, M. B. Martinez, B. A. Trump, J. D. Tarver, M. N. Dods, L. M. Funke, J. Börgel, J. A. Reimer, W. S. Drisdell, K. E. Hurst, T. Gennett, S. A. FitzGerald, C. M. Brown, M. Head-Gordon and J. R. Long, *J. Am. Chem. Soc.*, 2021, **143**, 14884–14894.

48 S. Biswas, M. Grzywa, H. P. Nayek, S. Dehnen, I. Senkovska, S. Kaskel and D. Volkmer, *Dalton Trans.*, 2009, **9226**, 6487–6495.

49 D. Denysenko, M. Grzywa, M. Tonigold, B. Streppel, I. Krkljus, M. Hirscher, E. Mugnaioli, U. Kolb, J. Hanss and D. Volkmer, *Chem.–Eur. J.*, 2011, **17**, 1837–1848.

50 P. Schmieder, D. Denysenko, M. Grzywa, B. Baumgärtner, I. Senkovska, S. Kaskel, G. Sastre, L. van Wüllen and D. Volkmer, *Dalton Trans.*, 2013, **42**, 10786–10797.

51 P. Schmieder, M. Grzywa, D. Denysenko, M. Hambach and D. Volkmer, *Dalton Trans.*, 2015, **44**, 13060–13070.

52 A. J. Rieth, Y. Tulchinsky and M. Dincă, *J. Am. Chem. Soc.*, 2016, **138**, 9401–9404.

53 H. Bunzen, M. Grzywa, R. Aljohani, H.-A. A. Krug von Nidda and D. Volkmer, *Eur. J. Inorg. Chem.*, 2019, **2019**, 4471–4476.

54 K. Knippen, B. Bredenkötter, L. Kanschat, M. Kraft, T. Vermeyen, W. Herrebout, K. Sugimoto, P. Bultinck and D. Volkmer, *Dalton Trans.*, 2020, **49**, 15758–15768.

55 L. Yun, C. Xin-Yi, Z. Kai, Z. Xue-Wen, Z. Dong-Dong, Z. Wei-Xiong, C. Xiao-Ming and Z. Jie-Peng, *CCS Chem.*, 2021, **4**, 1587–1596.

56 S. Biswas, M. Tonigold, M. Speldrich, P. Kögerler, M. Weil and D. Volkmer, *Inorg. Chem.*, 2010, **49**, 7424–7434.

57 Y.-Q. Lan, S.-L. Li, H.-L. Jiang and Q. Xu, *Chem.–Eur. J.*, 2012, **18**, 8076–8083.

58 R. Röß-Ohlenroth, M. Kraft, H. Bunzen and D. Volkmer, *Inorg. Chem.*, 2022, **61**, 16380–16389.

59 P. Q. Liao, H. Chen, D. D. Zhou, S. Y. Liu, C. T. He, Z. Rui, H. Ji, J. P. Zhang and X. M. Chen, *Energy Environ. Sci.*, 2015, **8**, 1011–1016.

60 Z. Chang, R.-B. Lin, Y. Ye, C. Duan and B. Chen, *J. Mater. Chem. A*, 2019, **7**, 25567–25572.

61 Y. Wang, N.-Y. Huang, X.-W. Zhang, H. He, R.-K. Huang, Z.-M. Ye, Y. Li, D.-D. Zhou, P.-Q. Liao, X.-M. Chen and J.-P. Zhang, *Angew. Chem., Int. Ed.*, 2019, **58**, 7692–7696.

62 Y. Xie, Y. Shi, H. Cui, R.-B. Lin and B. Chen, *Small Struct.*, 2022, **3**, 2100125.

63 D.-L. Chen, H. Shang, W. Zhu and R. Krishna, *Chem. Eng. Sci.*, 2014, **117**, 407–415.

64 B. Liang, X. Zhang, Y. Xie, R.-B. Lin, R. Krishna, H. Cui, Z. Li, Y. Shi, H. Wu, W. Zhou and B. Chen, *J. Am. Chem. Soc.*, 2020, **142**, 17795–17801.

65 Y. Xie, Y. Shi, E. M. Cedeño Morales, A. El Karch, B. Wang, H. Arman, K. Tan and B. Chen, *J. Am. Chem. Soc.*, 2023, **145**, 2386–2394.

66 Y. Ye, S. Xian, H. Cui, K. Tan, L. Gong, B. Liang, T. Pham, H. Pandey, R. Krishna, P. C. Lan, K. A. Forrest, B. Space, T. Thonhauser, J. Li and S. Ma, *J. Am. Chem. Soc.*, 2022, **144**, 1681–1689.

67 G.-D. Wang, H.-H. Wang, W.-J. Shi, L. Hou, Y.-Y. Wang and Z. Zhu, *J. Mater. Chem. A*, 2021, **9**, 24495–24502.

68 G.-D. Wang, Y.-Z. Li, W.-F. Zhang, L. Hou, Y.-Y. Wang and Z. Zhu, *ACS Appl. Mater. Interfaces*, 2021, **13**, 58862–58870.

69 Q. Zhang, G.-N. Han, X. Lian, S.-Q. Yang and T.-L. Hu, *Molecules*, 2022, **27**, 5929–5939.

70 D. Graham and G. McAnally, *Heterocycl. Commun.*, 1999, **5**, 377–378.

71 J. Rouquerol, P. L. Llewellyn and F. Rouquerol, *Stud. Surf. Sci. Catal.*, 2007, **160**, 49–56.

72 K. S. Walton and R. Q. Snurr, *J. Am. Chem. Soc.*, 2007, **129**, 8552–8556.

73 P. Iacomi and P. L. Llewellyn, *Adsorption*, 2019, **25**, 1533–1542.